



Calhoun: The NPS Institutional Archive
DSpace Repository

Theses and Dissertations

1. Thesis and Dissertation Collection, all items

2016-06

Investigation of the emissivity and suitability of a carbon thin film for terahertz absorbers

Sullivan, Naomi C.

Monterey, California: Naval Postgraduate School

<http://hdl.handle.net/10945/49394>

This publication is a work of the U.S. Government as defined in Title 17, United States Code, Section 101. Copyright protection is not available for this work in the United States.

Downloaded from NPS Archive: Calhoun



Calhoun is the Naval Postgraduate School's public access digital repository for research materials and institutional publications created by the NPS community. Calhoun is named for Professor of Mathematics Guy K. Calhoun, NPS's first appointed -- and published -- scholarly author.

Dudley Knox Library / Naval Postgraduate School
411 Dyer Road / 1 University Circle
Monterey, California USA 93943

<http://www.nps.edu/library>



NAVAL POSTGRADUATE SCHOOL

MONTEREY, CALIFORNIA

THESIS

INVESTIGATION OF THE EMISSIVITY AND
SUITABILITY OF A CARBON THIN FILM FOR
TERAHERTZ ABSORBERS

by

Naomi C. Sullivan

June 2016

Thesis Advisor:

Dragoslav Grbovic

Thesis Co-Advisor:

Fabio Alves

Approved for public release; distribution is unlimited

THIS PAGE INTENTIONALLY LEFT BLANK

REPORT DOCUMENTATION PAGE			Form Approved OMB No. 0704-0188	
Public reporting burden for this collection of information is estimated to average 1 hour per response, including the time for reviewing instruction, searching existing data sources, gathering and maintaining the data needed, and completing and reviewing the collection of information. Send comments regarding this burden estimate or any other aspect of this collection of information, including suggestions for reducing this burden to Washington headquarters Services, Directorate for Information Operations and Reports, 1215 Jefferson Davis Highway, Suite 1204, Arlington, VA 22202-4302, and to the Office of Management and Budget, Paperwork Reduction Project (0704-0188) Washington DC 20503.				
1. AGENCY USE ONLY (Leave Blank)		2. REPORT DATE June 2016	3. REPORT TYPE AND DATES COVERED Master's Thesis	
4. TITLE AND SUBTITLE INVESTIGATION OF THE EMISSIVITY AND SUITABILITY OF A CARBON THIN FILM FOR TERAHERTZ ABSORBERS			5. FUNDING NUMBERS	
6. AUTHOR(S) Naomi C. Sullivan				
7. PERFORMING ORGANIZATION NAME(S) AND ADDRESS(ES) Naval Postgraduate School Monterey, CA 93943			8. PERFORMING ORGANIZATION REPORT NUMBER	
9. SPONSORING / MONITORING AGENCY NAME(S) AND ADDRESS(ES) N/A			10. SPONSORING / MONITORING AGENCY REPORT NUMBER	
11. SUPPLEMENTARY NOTES The views expressed in this document are those of the author and do not reflect the official policy or position of the Department of Defense or the U.S. Government. IRB Protocol Number: N/A.				
12a. DISTRIBUTION / AVAILABILITY STATEMENT Approved for public release; distribution is unlimited			12b. DISTRIBUTION CODE	
13. ABSTRACT (maximum 200 words) The main goal of this work is to optimize the emissivity of terahertz (THz) thermal sensors by deposition of a carbon thin film. Previously, these thermal sensors were designed to detect THz radiation utilizing metamaterials in a complicated optical probing scheme. We have repurposed them to absorb terahertz radiation, convert the radiation to heat, and convey that surface temperature as an infrared image, essentially mapping the terahertz domain. This design has the potential to be used for optical applications such as an attachable lens that would convert any IR (infrared) camera into a THz camera. Additionally, by using this technique, we show that carbon thin films produce sufficient spectral emissivity for IR-based readout. We ascertained that to deposit a carbon thin film an iron catalyst is needed; pure aluminum cannot be used as a catalyst for chemical vapor deposition (CVD) of carbon. Overall, this study provides a viable method to fabricate thin carbon films at low temperatures for IR-based readout.				
14. SUBJECT TERMS MEMS, etching, EDS			15. NUMBER OF PAGES 73	
			16. PRICE CODE	
17. SECURITY CLASSIFICATION OF REPORT Unclassified	18. SECURITY CLASSIFICATION OF THIS PAGE Unclassified	19. SECURITY CLASSIFICATION OF ABSTRACT Unclassified	20. LIMITATION OF ABSTRACT UU	

NSN 7540-01-280-5500

Standard Form 298 (Rev. 2-89)
Prescribed by ANSI Std. Z39-18

THIS PAGE INTENTIONALLY LEFT BLANK

Approved for public release; distribution is unlimited

**INVESTIGATION OF THE EMISSIVITY AND SUITABILITY OF A
CARBON THIN FILM FOR TERAHERTZ ABSORBERS**

Naomi C. Sullivan
Lieutenant, United States Navy
B.S., Vanderbilt University, 2010

Submitted in partial fulfillment of the
requirements for the degree of

MASTER OF SCIENCE IN APPLIED PHYSICS

from the

**NAVAL POSTGRADUATE SCHOOL
June 2016**

Approved by: Dragoslav Grbovic
Thesis Advisor

Fabio Alves
Thesis Co-Advisor

Kevin Smith
Chair, Department of Physics

THIS PAGE INTENTIONALLY LEFT BLANK

ABSTRACT

The main goal of this work is to optimize the emissivity of terahertz (THz) thermal sensors by deposition of a carbon thin film. Previously, these thermal sensors were designed to detect THz radiation utilizing metamaterials in a complicated optical probing scheme. We have repurposed them to absorb terahertz radiation, convert the radiation to heat, and convey that surface temperature as an infrared image, essentially mapping the terahertz domain. This design has the potential to be used for optical applications such as an attachable lens that would convert any IR (infrared) camera into a THz camera. Additionally, by using this technique, we show that carbon thin films produce sufficient spectral emissivity for IR-based readout. We ascertained that to deposit a carbon thin film an iron catalyst is needed; pure aluminum cannot be used as a catalyst for chemical vapor deposition (CVD) of carbon. Overall, this study provides a viable method to fabricate thin carbon films at low temperatures for IR-based readout.

THIS PAGE INTENTIONALLY LEFT BLANK

Table of Contents

1	Introduction	1
1.1	Terahertz	1
1.2	Thermal Sensor	2
1.3	Related Work	7
2	Background	13
2.1	Blackbody Radiation	13
2.2	Measurement Techniques	17
3	Fabrication and Etching	19
3.1	Micro-Fabrication Process	19
3.2	Experiment 1: Etching	21
4	Results and Analysis	27
4.1	Experiment 2: Carbonization.	27
4.2	Experiment 3: Emissivity Test	38
5	Conclusions and Future Research	43
5.1	Conclusion	43
5.2	Future Research	43
	Appendix A Bosch Etch	45
A.1	Bosch Etching	45
	Appendix B Carbonization	47
B.1	Carbonization	47
	List of References	51

List of Figures

Figure 1.1	THz Spectrum.	2
Figure 1.2	Thermal Sensor Diagram.	3
Figure 1.3	Responsivity vs Thermal Conductivity.	6
Figure 1.4	Dissertation Results Composed by B. Kearney.	7
Figure 1.5	THz Bimaterial Sensors Simulated by Dr. Alves.	8
Figure 1.6	Metal-organic Hybrid Metamaterial Translators Fashioned by Dr. Grbovic.	9
Figure 1.7	Previous Terahertz Optical Readout Scheme.	10
Figure 1.8	Schematic Diagram of the Optical Readout to be used for Real-time THz Imaging.	11
Figure 2.1	Planck Blackbody Radiation Spectrum.	13
Figure 2.2	Nanoscale Soot Particles.	16
Figure 3.1	Fabricated THz Bi-material Sensor.	19
Figure 3.2	Metamaterial THz Thermal Translator Sensor.	20
Figure 3.3	SEM Image of Wafer after Bosch-Etched 150 Cycles.	22
Figure 3.4	SEM Image of Wafer after Bosch-Etched 580 Cycles.	24
Figure 3.5	SEM Image of Wafer after Bosch-Etched 550 Cycles.	24
Figure 4.1	Thermogravimetric Analysis.	28
Figure 4.2	SEM Image of Sample before Carbonization.	29
Figure 4.3	SEM Image of Sample after Carbonization.	30
Figure 4.4	Pixelated Sample Determined by EDX Analysis.	31
Figure 4.5	Carbon Thin Film Elemental Breakdown.	33

Figure 4.6	Third Carbonized Sample with Fe.	34
Figure 4.7	Second Carbon Thin Film Elemental Breakdown.	35
Figure 4.8	SEM Sample without Fe.	36
Figure 4.9	Percentages of Carbon Present in Sample 3 & 4.	38
Figure 4.10	Optical Scheme to Produce Emissivity Results.	39
Figure 4.11	Graph of Emissivity Results.	42
Figure B.1	Mold Used for Carbonization.	47
Figure B.2	Mold being Prepared for Use in the Furnace	48
Figure B.3	Gas Flow Arrangement.	48

List of Tables

Table 4.1	EDS Data from the Right Hand Side of Figure 4.3.	31
Table 4.2	EDS Data from the Left Hand Side of Figure 4.3.	32
Table 4.4	EDS Data from Left Hand Side of Figure 4.6.	34
Table 4.3	EDS Data from Right Hand Side of Figure 4.6.	35
Table 4.5	EDS Data from Right Hand Side of Figure 4.8.	36
Table 4.6	EDS Data from Left Hand Side of Figure 4.8.	37
Table 4.7	Emissivity Values at 35°C, 40°C, and 45°C.	41

THIS PAGE INTENTIONALLY LEFT BLANK

List of Acronyms and Abbreviations

CVD	Chemical Vapor Deposition
CNP	Carbon Nanoparticles
CNS	Carbon Nanostructures
DDSC	Derivative Differential Scanning Calorimeter
DSC	Differential Scanning Calorimeter
EDX	Energy-Dispersive X-ray Spectroscopy
FEL	Free Electron Laser
FPA	Focal Plane Array
FTIR	Fourier Transform Infrared Spectrometer
ICP	Inductively Coupled Plasma
IR	Infrared
MEMS	Microelectromechanical Systems
NEP	Noise Equivalent Power
PECVD	Plasma Enhanced Chemical Vapor Deposition
QCL	Quantum Cascade Laser
rms	root mean square
ROI	Region of Interest
RF	Radio-Frequency
SEM	Scanning Electron Microscope
TG	Thermogravimetry

THz Terahertz

Acknowledgments

Without the help and support of the following people, my thesis would not have been possible.

First and foremost, I would like to thank GOD for his unconditional guidance and wisdom.

I am also immensely grateful to Professor Grbovic, my thesis advisor, who provided essential technical support. I am thankful for his guidance and helpful feedback. His support and advice helped me tremendously during the preparation of my thesis.

My sincere appreciation goes to Dr. Fabio Alves for sharing his invaluable knowledge with me and for his time and effort used for the set-up of the optical schemes used in this research. A special acknowledgment goes out to Andreas Jacobke for all his work assisting me in the clean room and to Jeff Catterlin for his sage advice.

I would also like to thank Professor Claudia Luhrs for her insight and expertise that greatly assisted the research, Professor Sarath Menon for all the time he took out of his day to assist in EDX analysis, and Charliean Dominguez for her help carbonizing the sensors.

Last, but not least, I would like to thank my parents and my fiancé who continue to support me; a special debt of gratitude is due.

THIS PAGE INTENTIONALLY LEFT BLANK

CHAPTER 1:

Introduction

As science and technology progress to micro and nanoscopic dimensions, new fabrication methods are being used to engineer devices with ever increasing performance. Silicon, a primary substrate material, is used in many microelectromechanical systems (MEMS) devices due to its accessibility, high melting point, and low cost. Different micromachining techniques, such as deposition and etching silicon-based films and silicon wafers, can create a large array of designs and structures. This work uses techniques such as silicon etching and deposition in an attempt to provide performance improvements to terahertz (THz) sensors discussed in greater detail in later chapters. Terahertz sensors are devices designed to respond to electromagnetic radiation in the THz frequency spectrum, a spectrum until recently inaccessible. Prior to addressing improvements made however, this text will provide a theoretical foundation behind the motivation of experiments conducted herein. Therefore, this study will be preceded by an introduction to the THz spectrum, thermal sensors, and past research. This work also includes background information, such as blackbodies, emission, and software used. These concepts will be assembled as building blocks to construct a process which has the potential to lead to applications, such as a simple, screw-on attachment to a regular IR camera that would convert any IR camera into a THz camera via a removable attachment.

1.1 Terahertz

The terahertz imaging sensors operate in the region of the electromagnetic spectrum between microwave and IR (Figure 1.1). There is a renewed interest in exploiting the THz region especially for imaging techniques because it is non-ionizing; and hence, relatively harmless to biological tissue. THz applications include security screening, detection of harmful chemicals and bio-agents, and medical imaging. THz sources are difficult to obtain because they require complex, expensive equipment such as vacuum electronics, external pump lasers, or cryogenic cooling [1]. Typical sources of THz are free electron lasers (FELs), quantum cascade lasers (QCLs), and diode

based oscillators.

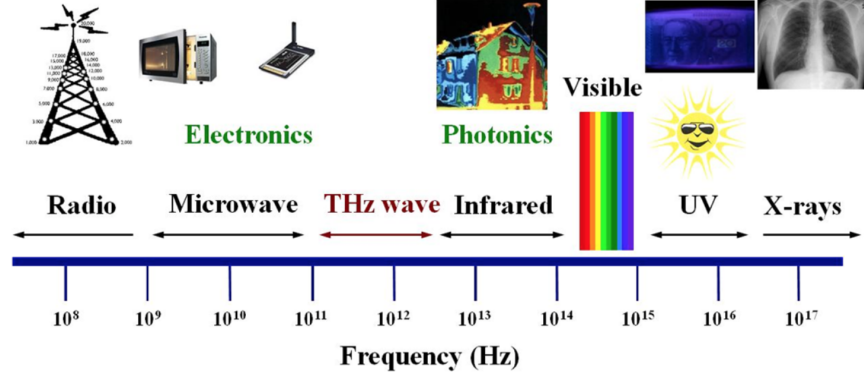


Figure 1.1: Location of the THz band within the Electromagnetic Spectrum.
Source: [2].

Unlike THz radiation, we encounter infrared light every day in common household appliances such as incandescent lightbulbs and IR light-emitting diodes in the television’s remote control [3]. It is most often felt as heat transfer via radiation. “Everything with a temperature above 5 degrees kelvin emits IR radiation” with frequencies ranging from 3 GHz to 400 THz [3]. A common way to detect infrared radiation, which will be used in subsequent experiments, is using an infrared camera. Out of the seven spectra, the focus in this work is on the THz and infrared regions.

1.2 Thermal Sensor

There are recent advancements in technology that use terahertz-to-infrared for imaging purposes. One such advancement is the use of uncooled thermal sensors for infrared images. Thermal imaging sensors are sensitive to temperature changes. There are certain parameters that are important to understanding thermal sensors; we will label them G, W, and C. Typically, the sensor is connected to a heat sink which absorbs and dissipates excess heat. The amount of heat loss to the heat sink is controlled by the thermal conductance (G) of the bridge or legs connecting them. The heat balance equation describes the relationship between these parameters,

$$W = G\Delta T + C \frac{d}{dt} \Delta T \quad (1.1)$$

where ΔT is the change in temperature due to incident power (W) and (C) is the sensor's thermal capacitance. The left hand side of Equation (1.1) is total power, the first term on the right represents loss or leakage, and the second term on the right represents the temperature storage of the sensor [4]. A graphical representation of Equation (1.1) is shown in Figure 1.2.

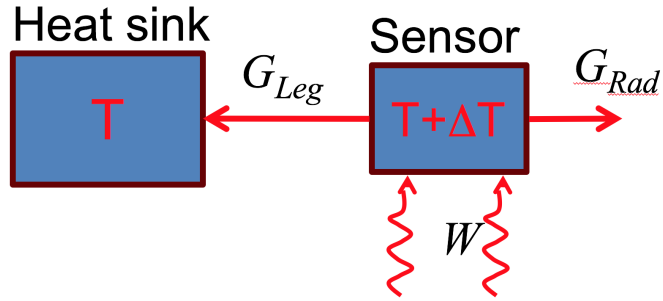


Figure 1.2: Graphic depicting the main components of a thermal sensor and the heat exchange it has with its environment. The diagram shows incoming power, W , creating a temperature difference, ΔT , between the sensor and the heat sink at temperature T . Source: [4].

The main components of thermal detectors are: an absorber (sensor itself), thermal connectors (G_{Leg}), and a substrate (heat sink). Note that the G in Equation (1.1) is $G_{Leg} + G_{Rad}$ in Figure 1.2. $G_{convection}$, or convection loss, can be controlled through the gas pressure of the surrounding environment and will be ignored because the sensors are operating at low pressures [5]. Moreover, under steady state conditions, the temperature of the sensor relative to the heat sink is given by

$$\Delta T = \frac{W}{G} \quad (1.2)$$

This equation implies that to achieve higher sensitivity, a smaller G is desirable.

When the radiation flux is removed, Equation (1.1) goes to zero. Using separation of variables we can derive the following relationship

$$\Delta T = \frac{W}{G} e^{-\left(\frac{t}{\tau}\right)} \quad (1.3)$$

where $\tau = \frac{C}{G}$ and is known as the thermal time constant. Thermal detectors are generally slow with the time constant in the milliseconds [4]. A faster response time is achievable by increasing the thermal conductance (G) with the heat sink. However, this will reduce the highest temperature that the sensor can achieve (W/G). This trade-off must be considered and can be properly tuned according to application demands.

Moreover, the frequency response of the thermal detector is found by replacing the constant incident power with a frequency dependent expression, $W = W_o e^{i2\pi ft}$ and $\Delta T = \Delta T_o e^{i2\pi ft}$ [4]. Plugging in these two expression into Equation (1.1) yields

$$\Delta T_o = \frac{W_o}{G} \frac{1}{\sqrt{1 + (2\pi f \tau)^2}} \quad (1.4)$$

Equation (1.4) is the frequency response equation for a thermal conductor which reiterates the W/G relationship. When graphing ΔT vs frequency, the resultant graph resembles a low-pass filter. The graph depicts when the response begins to fall off, which correlates to frequencies less than $\frac{1}{2\pi\tau}$ [4].

1.2.1 Figures of Merit

There are two important parameters used to quantify the performance of the terahertz imaging sensors: responsivity and detectivity [4]. Responsivity measures how big the output is compared to the input of the detector. Detectivity measures the effective ability of detecting signal over noise. The materials and dimensions of the original THz device were chosen based on these parameters. This study aims to change the dimensions of these devices, which in turn will affect the performance of the sensor.

Determining whether the modification to the sensor will lead to desirable results is the ambition of this study.

Responsivity

The responsivity of a detector under a sinusoidal illumination power, as described by [5], is

$$R_{th} = \frac{\Delta T}{W_o} = \frac{\eta}{G\sqrt{(1 + \omega^2\tau^2)}} \quad (1.5)$$

where η is the absorbance, W_o is incident power absorbed by the sensitive region of the detector, and ω is the angular modulation frequency of the incident radiation. Equation (1.4) elucidates that minimizing τ will increase responsivity. To minimize τ ($\tau = \frac{C}{G}$), C should be minimized. The thermal capacitance, C , depends on the volume of the detector. The area of the thermal sensor is usually determined by the wavelength of interest. The thickness of the thermally sensitive area should be as thin as possible in order to reduce the volume and reduce C . Reducing capacitance minimizes τ . The thermal time constant must be minimized for real time imaging applications; detectors usually operate in the frequency range where $\omega\tau \ll 1$ [5]. The THz device has already incorporated these design features suitable for real time imaging; therefore, the size of the detector will not be manipulated. However, this study will add a carbon thin film to the back end of the THz sensor (the purpose will be revisited in detail in later chapters); therefore, the volume of the thermally sensitive region will increase which will increase thermal capacitance. Although an increase in thermal capacitance is undesirable, it may be overwhelmed in a change in thermal conductance that can lead to a desirable result. Looking at Equation (1.4) once more, another option that is available that will increase responsivity is to reduce the thermal conductance (Figure 1.3).

Figure 1.3 shows that decreasing thermal conductance increases responsivity. The catch is that the thermal conductance cannot be indefinitely decreased. This concept is embodied in Kirchoff's law which ensures that radiation losses are unavoidable, hence thermal conductance of zero is not feasible [5]. Measured values of thermal

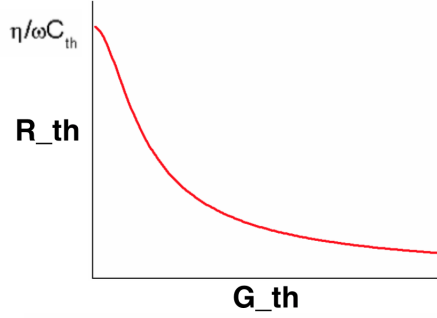


Figure 1.3: A graph of Responsivity [K/W] vs Thermal conductivity [W/K] in a thermal sensor under sinusoidal illumination power. R_{th} increases with higher absorption (η), lower frequencies (ω), and smaller C. Source: [5].

conductance for similar THz thermal sensors are around $9.81 \times 10^{-8} \left(\frac{W}{K}\right)$ to $3.26 \times 10^{-7} \left(\frac{W}{K}\right)$ [6]. With a carbon thin film, smaller thermal conductance is anticipated.

Detectivity

The second parameter is detectivity. Detectivity of a detector is inversely proportional to the noise equivalent power. The following is an expression for specific detectivity

$$D^* = \frac{\sqrt{A\Delta f}}{NEP} \quad (1.6)$$

where Δf is the bandwidth of the amplifier, A is the area of the detector, and noise-equivalent power (NEP) is the root mean square (rms) incident radiant power that gives a signal equal to the noise signal (i.e., signal-to-noise ratio of one) [4]. Higher signal-to-noise ratio which corresponds to a smaller NEP gives a better probability of detection. Noise sources for a thermal sensor include temperature fluctuation noise, background fluctuation noise, and thermomechanical noise [7]. In an ideal thermal detector the only noise is thermal fluctuation, which is due to heat loss to the heat sink [8]. However, no detector is ideal, and each detector will have noise arise from additional sources such as when there is signal loss due to “incomplete absorption at the surface and any transmission losses by the optical system.” [8]

This research does not elaborate on detectivity; however, the understanding that the introduction of a carbon thin film could reduce signal loss and will result in a change in thermal fluctuations is important to the performance of the terahertz imaging sensors.

1.3 Related Work

Past research at NPS focused on improving the thermal detectors' THz absorption without compromising their real-time imaging performance. Studies probed the integration of a metamaterial into a bi-material sensor to accomplish this goal. The THz metamaterial absorbers are composed of a “metal layer patterned into a periodic array of squares separated from a ground plate of continuous metal by a dielectric spacer” [5] (Figure 1.4).

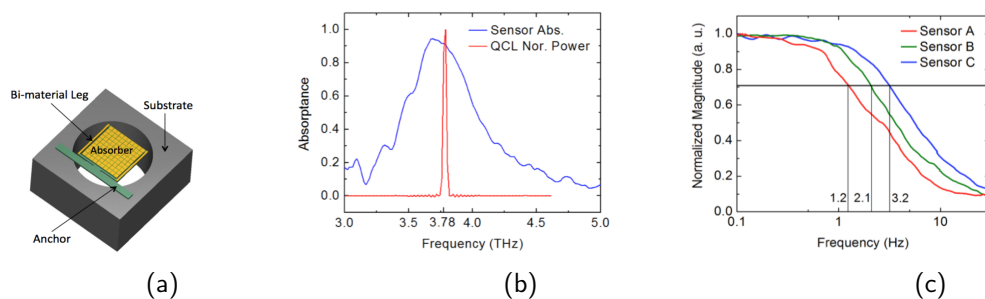


Figure 1.4: (a) 3D view of the THz bi-material sensor with integrated metamaterial absorber, fabricated on a Si substrate. (b) Measurement of the absorption spectra of the THz sensors material structure (blue line) compared with the QCL normalized emission (red line). (c) Normalized frequency responses for the three sensors tested (colored lines). The time constants were retrieved by taking the inverse of the 3 dB frequencies that are 1.2, 2.1 and 3.2 rad/s for sensor A, B, and C, respectively. Source: [5].

The results were promising; and in particular, [5] details the accomplishments made by the NPS research team. Conclusions in [5] include but are not limited to the peak absorption frequency was inversely proportional to the dimensions of the squares; and by changing the unit cell structure, the metamaterial absorbers could be used as “absorbing layers in thermal imagers [paired] with narrow-band sources to significantly

enhance their sensitivity through resonant absorption at the emitter frequency.” [5], [9] The results of [5] have been summarized in Figure 1.4.

According to [5], the metamaterial structures provided near 100% absorption at 3.8 THz with a responsivity value of $1.2 \frac{\text{deg}}{\mu\text{W}}$ and a time constant of 200 ms (Figure 1.4). The authors concluded that the sensors were not optimized for imaging, but ventured to obtain raw images of the QCL beam [5]. Figure 1.5 shows the optimized design from a successive paper [10], which expanded on research reported in [5].

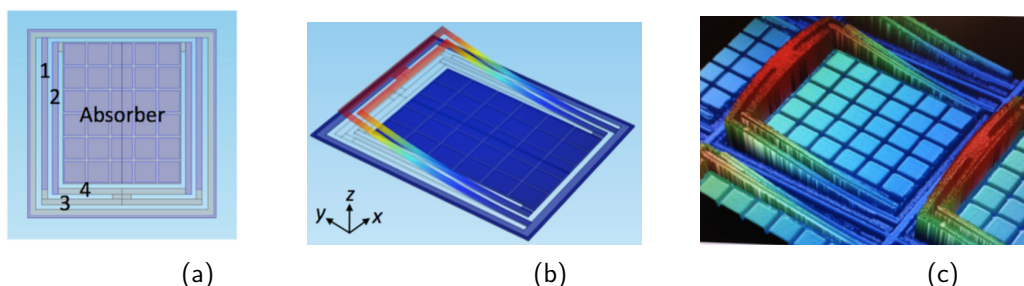


Figure 1.5: Stimulated fabricated and measured self-leveling THz bimaterial sensors. (a) Top view where the central absorber is $100 \times 120 \mu\text{m}$, and the pixel size is $160 \times 160 \mu\text{m}$. Two legs on each side consist of bimaterial segments (1 and 2) and thermal insulating segments (3 and 4). The segment 1 is connected to the substrate (heat sink) and consequently thermally shorted. (b) 3-D simulation of sensor. (c) Measured 3-D profile showing stress compensation. Source: [10].

The paper investigated the optimal configuration of the sensors, the bi-material legs, and the anchor that would maximize responsivity. These configurations were probed via optical readout. The fabricated sensors are designed to have a membrane that dissipates heat by introducing a metallic frame around each pixel [10]. The pixels area is 15 times smaller than previous generations in order to create a small pitch; [10] states that “the absorbing area occupies 50% of the pixel, as opposed to 20% in the previous sensor.” According to [10], the sensor’s responsivity value is $0.75 \frac{\text{deg}}{\mu\text{W}}$, and its time constant is 150 ms. These values are comparable to values reported in [5]. Furthermore, this paper coupled the fabricated THz FPAs to an optical readout system producing a real time THz image. Using this imaging system, it was concluded that the detector’s frequency response can be tuned and “the sensitivity and resolution

can be set according to imaging demands.” [10]

These THz sensors were also studied in a follow-on paper [6]. The authors optimized the devices by converting the bimaterial device to band translators. SU8-based MEMS THz FPAs are introduced because this modification would make the fabrication process easier and cost less [6]. Figure 1.6 is an illustration of the optimized sensor.

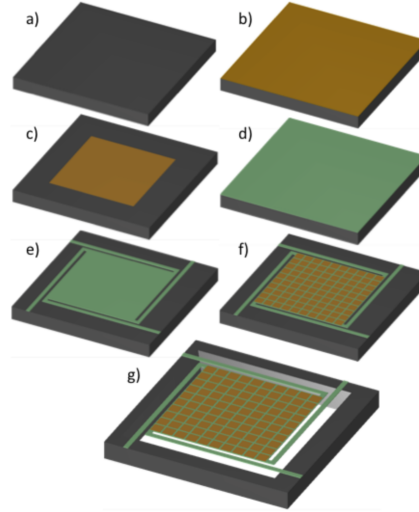


Figure 1.6: Depicts a sequence of steps for making metal-organic hybrid metamaterial translators. (a) Double-sided polished wafer. (b) Deposition of 100nm aluminum film. (c) Ground planes are patterned and etched. (d) Deposition of 500nm of SU-8. (e) SU-8 is photolithographically patterned, developed, and hard baked. (f) Deposition of second metal layer via thermal evaporation and patterning of resonant squares. (g) bottom opening are patterned and released via BOSCH etch. Source: [6].

Research in [6] studied two devices: a metal-dielectric metamaterial device (Si/Al/ SiO_x /Al) and a metal organic hybrid thermal translator (Si/Al/SU-8/Al). The thermal conductance (G) of these devices were calculated to be $3.26 * 10^{-7} \left(\frac{W}{K} \right)$ and $9.81 * 10^{-8} \left(\frac{W}{K} \right)$, respectively [6]. As described by [6], the responsivity was found to be $3.1 \left(\frac{K}{\mu W} \right)$ and $12 \left(\frac{K}{\mu W} \right)$ with time constants of 358 ms and 1.28 s for the respective devices. In both cases, metal-dielectric and metal-organic sensors, the temperature of each pixel must be read by an infrared camera. The main problem found in both cases is that the back side of the sensors, used for temperature readout, are metallic;

and therefore, exhibit very low emissivity. One possible way to increase the emissivity of the readout layer is to deposit a carbon film, which by nature exhibits higher emissivities [11]. The objective of this thesis is to investigate the processes of carbon deposition and the impact of this film on emissivity and other properties of the sensor.

1.3.1 Readout Schemes

Drawing from previous research, [10], THz imagers were fabricated with metamaterial absorbers and metal-coated legs that would deform when their temperature changes, rotating the reflective side of the absorber so that they could be optically probed when they rotated. The readout process for these THz imagers was complex (Figure 1.7).

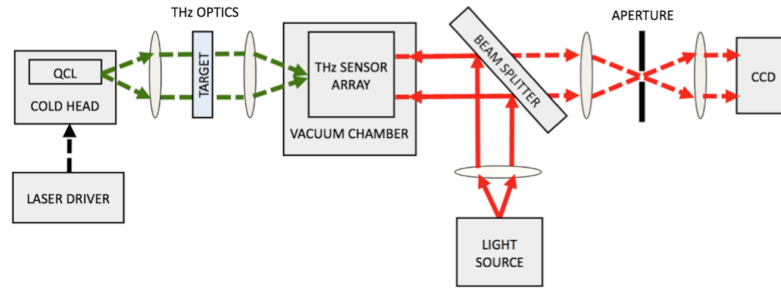


Figure 1.7: Schematic diagram of the optical readout used for real-time THz imaging with the fabricated THz FPA. Green lines represent THz waves and red lines represent visible light. Source: [10].

Over a couple of evolutions, the THz scheme was modified by researchers in [6] to include an IR camera (Figure 1.8).

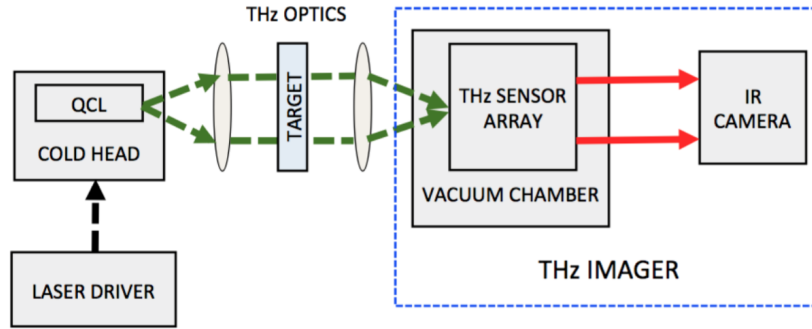


Figure 1.8: Schematic diagram of the optical readout used for real time Thz imaging with the fabricated THz FPA. Source: [6]

In Figure 1.8, “the QCL THz beam is collimated and passes through the imaging target (scene) and then re-focused on the THz FPA” via tsurupica or polyethylene lenses [6]. Further elaboration by [6] states, “The Thz FPA sensors placed inside the vacuum chamber, heat up proportionally to the transmissivity/absorptivity of the target at the QCL frequency.” A thermal, uncooled IR camera is used to read the sensor pixel that has been heated, and an IR imaging system manages the software and image-processing [6]. This infrared readout is much simpler than the optical readout previously used (Figure 1.7) and the sensor can be used as a simple screw-on attachment for IR cameras to “see” THz scenes.

THIS PAGE INTENTIONALLY LEFT BLANK

CHAPTER 2:

Background

This chapter lays the theoretical foundation behind the motivation for adding a carbon layer to the THz sensor as well as the experimental schemes for sensor characterization. Blackbody radiation is explained through well-established equations and concepts in order to show the importance of emissivity on the readout scheme proposed in this research. Measurement techniques are also discussed.

2.1 Blackbody Radiation

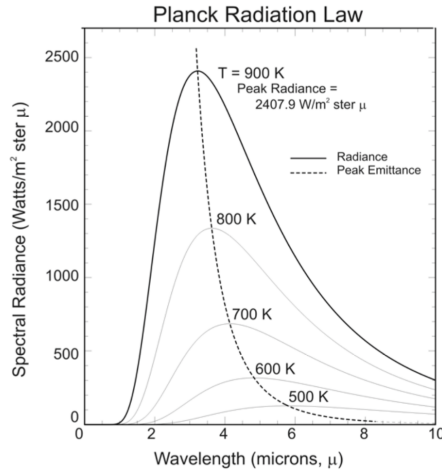


Figure 2.1: Planck black body radiation has a certain spectrum and intensity that depends only on the temperature of the body. As the temperature decreases, the peak moves to longer wavelengths at lower intensities. Source: [12].

Blackbody radiation refers to a hypothetical body that simultaneously absorbs and emits all incoming radiation at a given temperature and frequency while maintaining thermal equilibrium. A widely used model to approximate a blackbody is to have a small hole in a cavity at a fixed temperature with walls that are insulators. The cavity is created in such a way that properties attributed to it are non-consequential when

recording the results. Incident radiation that is at a wavelength smaller than the hole is able to pass through the hole and becomes trapped in the cavity. Only a very small amount of radiation will escape and that escaping radiation will approximate blackbody radiation which relies only on temperature and energy characteristics. Plank discovered the formula describing the blackbody emission spectrum. The continuous distribution as shown by Planck radiation law can be seen in Figure 2.1. Planck's Law can describe spectral radiance for monochromatic light of emitted radiation of a blackbody as a function of surface temperature.

2.1.1 Spectral Emittance

Planck's radiation law illustrated in Figure 2.1 can be mathematically expressed by two different equations: photon flux emittance and spectral emittance [4]. Looking at spectral emittance (M) as a function of wavelength, the power flow of thermal radiation through an area (A) in the cavity is given by

$$M(\lambda, T) = \frac{2\pi hc^2}{\lambda^5} \frac{1}{\exp(\frac{hc}{\lambda kT}) - 1} \quad (2.1)$$

where h is Planck's constant ($6.6260693 \times 10^{-34} \text{ W s}^2$), c is the speed of light ($2.99792458 \times 10^8 \text{ m s}^{-1}$), λ is the wavelength (m), and k is Boltzmann's constant ($1.380658 \times 10^{-23} \text{ J K}^{-1}$). Equation (2.1) represents the spectral emittance equation which has units of $(\frac{W}{m^2})$.

2.1.2 Total Power Emitted

From the spectral emittance equation, $M(\lambda, T)$, three important equations can be derived: total power, net power, and max wavelength. The total power emitted is represented by the area under the curve (Figure 2.1). Mathematically, the total power emitted by a blackbody per unit area can be obtained by integrating the spectral emittance curve over all wavelengths [4]:

$$M_e(T) = \int_0^\infty M(\lambda, T) d\lambda = \frac{2\pi^5 k^4}{15c^2 h^3} T^4 = \sigma T^4 \quad (2.2)$$

The resulting equation which describes the power radiated from a blackbody is known as the Stefan Boltzmann law in which the units are ($\frac{W}{m^2}$). The Stefan-Boltzmann constant, σ is equal to $5.67 \cdot 10^{-8} \frac{W}{m^2 K^4}$. T is the temperature of the radiator in kelvin. Note that absolute temperature is the most important parameter for blackbodies because Equation (2.2) is stating that the power emitted per unit area of the surface of a blackbody is directly proportional to the fourth power of its temperature.

Additionally, the net power radiated is given by

$$P_{net} = A\sigma\epsilon(T^4 - T_o^4) \quad (2.3)$$

where T_o is the temperature of the heat sink and ϵ is the emissivity. Emissivity of a surface is the measure of the efficiency in which the surface emits energy. Lastly, Wien's displacement law gives the wavelength at which the peak in radiation occurs (λ_{max}) and is obtained by reading the graph in Figure 2.1 where the derivative is equal to zero

$$\frac{\partial M_e(\lambda, T)}{\partial \lambda} \bigg|_{\lambda=\lambda_{max}} = 0 \quad (2.4)$$

$$\lambda_{max} = \frac{a}{T} \quad (2.5)$$

where a is a constant of $2.898 \cdot 10^{-3}$ with units of ($m \cdot K$) and λ_{max} is given in meters.

2.1.3 Carbon

Carbon, especially carbon soot, is very versatile with vast applications. In addition to carbon soot's favorable spectral radiance characteristics, this form of carbon is being investigated to power lithium batteries and to use in health applications [13]. Carbon soot is hydrophobic and has electrochemical properties which make it suitable to be used as an electrode. Researchers have investigated candle soot to power lithium ion batteries used in smartphones, cars, cameras, and airplanes [13]. Furthermore, carbon nanoparticles can become luminescent for cell imaging applications by simply treating

the candle soot with a reflux reaction and a strong oxidizing agent to disassociate the carbon particles and make them luminescent [14]. Although carbon is widely used, its radiation characteristics in the infrared make it remarkable. In this research, we will apply a carbon soot to the THz device just for its radiation characteristics. In addition to the carbon particles being dark already, the uneven surface due to different particle sizes of the carbon soot makes it even darker because “any light that reflects from one particle will hit another [particle] and get absorbed,” [15] as illustrated in Figure 2.2.

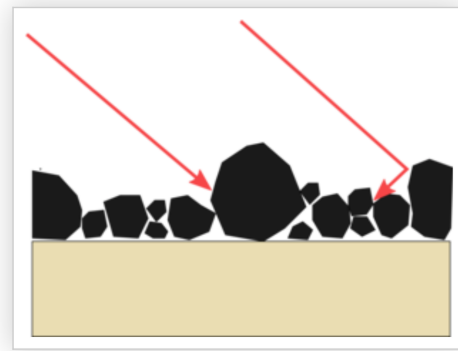


Figure 2.2: Soot is made up of different sized nano particles. These different sizes create a rough surface. When light hits the rough surface it will be reflected, hit another particle, and be absorbed. Source: [15].

2.1.4 Emissivity

Real infrared sources emit at lower powers than blackbodies. These sources can be characterized by higher emissivity. A blackbody has an emissivity $\epsilon = 1$, therefore it is a perfect emitter/absorber. According to a corollary of Kirchhoff’s law, which states that for “an arbitrary body emitting and absorbing thermal radiation in thermodynamic equilibrium, the emissivity is equal to the absorptivity.” [16] Therefore, a good absorber is a good emitter ($\alpha_\lambda = \epsilon_\lambda$). In comparison, a white body reflects rather than absorbs all incident radiation and has an emissivity $\epsilon = 0$, a perfect reflector. Emissivity is dependent upon the structure’s surface. Emissivity can be expressed by taking the source’s total power exitance divided by that of a blackbody at the same temperature:

$$\epsilon(\lambda, T) = \frac{M_e(\lambda, T)_{real\ source}}{M_e(\lambda, T)_{blackbody}} \quad (2.6)$$

Most objects do not fall into the white body/blackbody categories; however, any object that has a temperature above absolute zero will radiate thermal radiation. Therefore, most objects are considered grey bodies or bodies that radiate as blackbodies, but with an emissivity lower than 1. Different materials exhibit different emissivities. As a reference, most polished metals have emissivity values near 0.05 to 0.1 [17]. Oxidized metals have emissivity values of 0.3 to 0.9 [17]. Currently, metamaterial based absorbers are not good emitters in IR as their readout side is made out of aluminum with emissivity of ~ 0.03 [6]. Carbon is a highly emitting/absorbing layer, $\epsilon = 0.7 - 0.8$, as opposed to metal films which are great reflectors, not good emitters [18]. These qualities make a carbon thin film promising for applications such as heat dissipation in materials for terahertz use. Therefore, this research will investigate and measure the emissivity of a carbon film placed over the aluminum layer that is currently on the readout side of the terahertz devices.

2.2 Measurement Techniques

In addition to emission measurements, we conducted preliminary experiments using a X-ray microanalysis, technique on surrogate wafers with a thin, carbon film layer. These surrogate wafers are used to assess the adhesion of the organic layer to an aluminum substrate and afterwards they were used in the emissivity measurement experiments.

2.2.1 EDX

The measurement technique, X-ray microanalysis, is an analytical method used for elemental analysis. A scanning electron microscope (SEM) is used for electron beam excitation. These charged particles bombard the atoms in the sample. X-ray emission is stimulated when the inner shell electrons of the atom are excited and ejected from the shell creating holes that are filled by the outer shell electrons. The atom is said to be ionized because there was enough energy supplied to break the bond between the electron and the nucleus. Moreover, the X-rays emitted have fixed energies and can

be measured as peaks in the software analytical system. The transitions are named according to their initial and final level. For example, the K_α X-ray is a transition between the $n=2$ atomic orbital to $n=1$ atomic orbital [19].

The first to measure the frequencies of the X-rays emitted by certain elements was Henry Gwyn-Jefferies Moseley. His experimental data allowed him to use X-ray frequencies to infer each element's atomic number (Z). He found that the frequency, ν , of the K_α X-ray can be derived as

$$\nu^{1/2} = C(Z - \sigma) \quad (2.7)$$

where C and σ are constants specific to each X-ray emitted [20], and Z is the atomic number of the absorbing element. σ is known as the screening constant and varies for each series. For example, $\sigma = 1$ for the K series. The expression $(Z - 1)$ is the effective nuclear charge [20]. Not only can we find the series frequencies when the energy is given, but also determination of the atomic number is possible. Analysis of the voltage pulse produced, which is proportional to the incoming X-ray photon, determines the chemical composition of the sample. Our research capitalizes on this phenomena by using energy-dispersive X-ray spectroscopy (EDX) software to determine the chemical composition of our surrogate wafers [21]. EDX also ascertains the series frequencies for each elemental peak. Fortunately, the data generated has only the K_α series frequencies which will be identified in ensuing tables.

CHAPTER 3:

Fabrication and Etching

3.1 Micro-Fabrication Process

Fabrication of the terahertz device was done using standard micro-fabrication techniques. The THz devices were manufactured at Oak Ridge National Laboratory by Doctor Fabio Alves and Professor Dragoslav Grbovic with the exception of trenching the sensors and the growth of the carbon thin film, which was done at the Naval Postgraduate School.

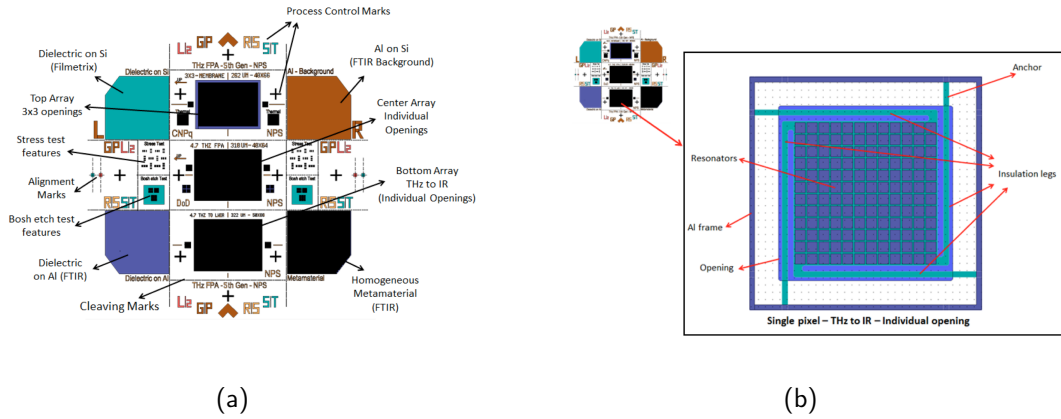


Figure 3.1: (a) Schematic of the fabricated focal-plane array THz bi-material sensor with integrated metamaterial absorber, fabricated on a Si substrate. (b) A zoomed in view of the THz to IR sensor. Source: [22].

Figure 3.1 illustrates the layout of the wafers with 3 focal plane arrays with a pixel size of $340\ \mu m$, absorber site of $200\ \mu m$, sensor of $18\ \mu m$, and leg width of $8\ \mu m$. The substrate is made of silicon and is $300\ +/-10\ \mu m$ thick. 90 nm of aluminum was deposited on top of the SiO_x layer creating a ground plate using the Angstrom Engineering Covap thin film metal deposition evaporator system. SPR 955-0.7 was spin-coated onto the wafer, patterned, and etched. Photoresist was stripped using oxygen plasma and the wafer was cleaned. Then, $1.2\ \mu m$ of SiO_x and 90 nm of aluminum were deposited. The aluminum was patterned with the resonator mask and

dry etched. Photoresist was stripped using oxygen plasma clean and the structure and legs were patterned. Finally, the bottom of the wafer was patterned to release the sensor structure (Figure 3.2).

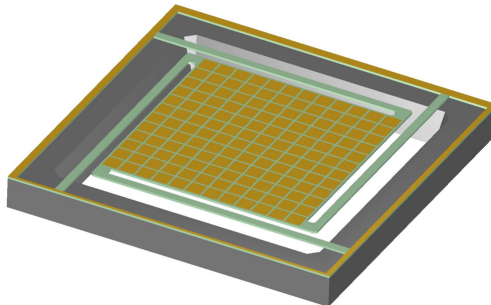


Figure 3.2: MEMS Pro generated design of the metamaterial THz thermal translator sensor with legs, a central resonator, openings, and pixel separation based on a metamaterial absorber. The z dimension of the substrate (grey) is scaled down for visual purposes. Source: [23].

After these sensors are released (Figure 3.2), the intention is to deposit a carbon film underneath the thermally sensitive region, which is the back side (ground plane side) of the sensor.

3.1.1 Plasma Etching

Etching removes material from a wafer's surface. There are two types of etching: wet and dry. Wet etching involves placing the wafer with a protective mask into a liquid solution. The etching is isotropic or directionally independent. Dry etching can be further subcategorized into ion etching, sputter etching, and vapor phase etching. The clean room at NPS features a specialized ion etcher which allows deep silicon etch (Bosch). This instrument can create depths of hundreds of microns with nearly vertical sidewalls and high aspect ratios [24]. It works in the following manner. The first gas composition deposits a polymer, in this case octafluorocyclobutane (C_4F_8), to the surface of the substrate. The polymer is used to protect the sidewalls. During the etching phase, directional ion bombardment attacks the bottom of the trench, sputtering the polymer away, but keeps the sidewalls intact. In the next phase, the

second gas composition is used, usually sulfur hexafluoride (SF_6). The bottom of the trench, which is now exposed, gets etched away at a faster etch rate than the sidewalls, which have been protected by the polymer because the polymer dissolves slowly in SF_6 . This process then repeats a predetermined number of times (cycles).

Points of Consideration for Etching

A key item to consider when etching is the etch rate or the speed of material removal. The higher the etch rate means faster production. A term called “aspect ratio dependent etching” explains the concept that as the aspect ratio of the etched trench increases, the etch rate slows down. [25] The directionality can either be anisotropic or isotropic. Isotropic is when the etch rate is equal in all directions. Another key item to consider is the etch rate selectivity. Selectivity is the ratio of the etch rate of the film to the etch rate of the substrate or mask [26]. This ratio has to be proportioned correctly to achieve the desired depth without compromising the integrity of the top structures on the sensor.

We used a dry etching technique with the Oxford Plasmalab System 100 DRIE for an anisotropic etch. The Oxford etcher is a reactive ion etching tool. The system uses a combination of gases, such as SF_6 , Ar , O_2 , C_4F_8 , and N_2 . These gases are fed into the system by a gas pod. The gas pod controls the flow of the gases and is controlled by system software. Nitrogen and helium cool and vent the chamber. The system operates under vacuum with loadlock exchanging the wafers. Chilled water cools the radio-frequency (RF) power generators. The RF power is applied to inductively coupled plasma (ICP) sources and substrate electrodes to generate the etch plasma [27].

3.2 Experiment 1: Etching

The manufacturing of the THz sensors was completed at Oak Ridge National Laboratory with the exception of the last step in the microfabrication process, trenching. An etch depth of 300 microns is required in order to release the device. The 300 micron demand is because the silicon wafers used are 300 microns. Backside trenching using the Bosch etch process exposes the absorber ground plane which will be coated with

carbon. In order to etch the sensor’s opening with a particular shape, it is necessary to apply a protective layer where etching is not desired. The protective layer used is positive photoresist called SPR220-7 which is used for applications that need thicker resist. This resist can be modified via photolithography. Photolithography is a process that involves multiple steps. The process begins with the deposition of a resist on the silicon wafer. Then, a mask with opaque features is brought close to the wafer with resist, light rays pass through the mask to the wafer, and regions that are not covered by the opaque features change the resist’s chemical composition. For positive resist, this change makes the resist more soluble in wet chemical developer. After developing the wafer, the wafer has been patterned, some areas have photoresist and others do not. The photoresist, which is now on specific areas of the wafer, is a mask that preserves the structure underneath it. For our purposes, we wanted to verify that 10 microns of SPR220-7 is sufficient to etch a depth of 300 microns in order to open up the device’s membrane. Understanding the etch rate and selectivity allows us to etch at the desired depth. Test sample wafers were fabricated to evaluate Bosch etch rates. The etching process begins when the wafer is loaded into the chamber via loadlock. The wafer is “mechanically or electrostatically clamped to the temperature-controlled lower electrode.” [27] Helium “pressure is applied to the back of the wafer to provide good thermal conductance between the chuck and the wafer.” [27] Appendix A shows the Bosch recipe. We fabricated a wafer composed of Si/SPR-2207, and Bosch etched it for 100 cycles. Selectivity was 1:35.5 with an etch rate per cycle into Si of 0.64. Figure 3.3 is an SEM image of the results.

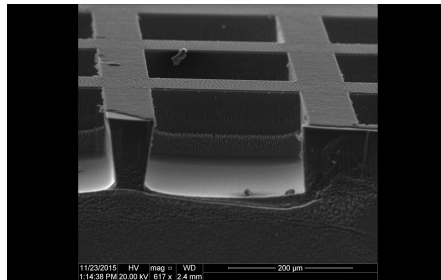
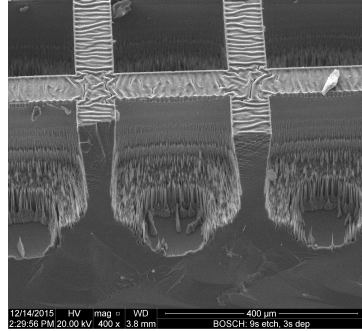


Figure 3.3: A scanning electron microscope (SEM) image of the bottom side of a wafer composed of Si/SPR-2207 after etching for 150 cycles. The image shows sidewalls slanted inward. Source: [28]

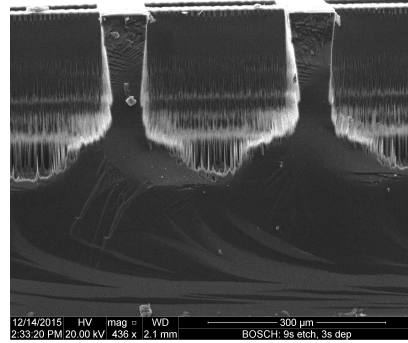
In Figure 3.3, the 50+100 cycles wafer image shows slightly slanted sidewalls with a uniform etch rate (i.e., no triangular shape). Note the “+” denotes that the etching process was done in increments. For example, in Figure 3.3, the wafer was first etched for 50 cycles, removed, and then it was placed back into the etcher for 100 more cycles. The NPS instruments are new and need characterization, so we proceeded to etch wafers composed of Si/SPR-2207 in increments to determine the etch rate and selectivity.

In order to create a greater depth in our trench, we ran another experiment. In this experiment, 10 microns of SPR-2207 is deposited to a double sided polished 300 micron silicon wafer using standard spin-coating procedures. The photoresist was patterned, developed, and hard baked for approximately 30 min. Subsequently, the wafer was placed in the Bosch etcher in increment sizes of 80 and 100 cycles until 300 microns was etched. We configured the Oxford etcher to Bosch etch at 9 sec etch rate and a 3 sec deposition rate. This etch method resulted in roughly 580 cycles. Figure 3.4 illustrates the results.

Selectivity of SPR-2207 to Si after the initial 100 cycles was 1:26. When the depths of the holes were about 100 μm (after 380 cycles), the selectivity of SPR-2207 to Si rose to 1:40. After the next two 100 cycle runs, selectivity stayed constant at 1:41 and 1:40, respectively. The etch rate was approximately 0.4. After viewing the results of the second experiment (Figure 3.4), the recommended way to improve the etching process was to make a few changes to the method of patterning. During this process we increased the exposure time setting from 400 to 500 and increased the post-exposure baking to 35+min before development. The exposure time is called integra (short for integration) time and is a user defined setting from 0.1 to 59.9 [29]. The light integrator is defined as $\frac{mJ}{cm^2}$ doses per unit [29]. Furthermore, in order to control the substrate temperature, we etched the wafer in increments of 50 cycles for a total of 550 cycles. This process maintained the chiller temperatures at 15°C. Temperatures in the chamber can range from -150°C to 400°C [27]. Maintaining the chiller temperatures at 15°C controls the substrate temperature. Typically, substrate temperatures have an effect on the etch results, namely the etch rate, selectivity and surface roughness. The results are depicted in Figure 3.5.

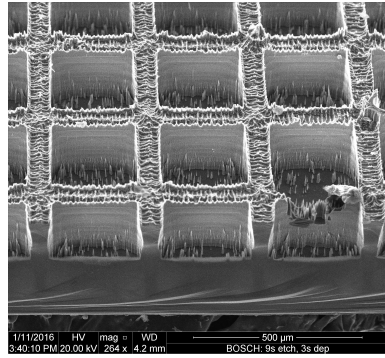


(a)

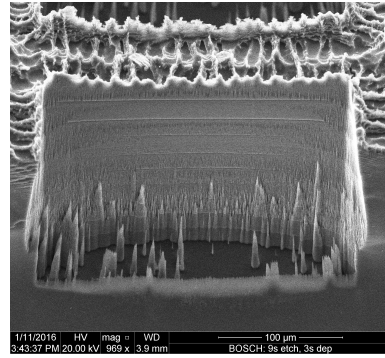


(b)

Figure 3.4: (a) and (b) are SEM images at 20kV of the same wafer composed of Si/SPR-2207 showed the formation of micro-pillars after 580 cycles with slightly slanted sidewalls. Source: [28].



(a)



(b)

Figure 3.5: (a) and (b) are SEM images at 20kV of the same wafer composed of Si/SPR-2207. The wafer showed micro-pillar formations after 550 cycles with slightly slanted sidewalls. Source: [28].

Figure 3.5 illustrates surface imperfections in the cavity with side walls that are nearly vertical. On average, selectivity of SPR-2207 to Si was similar to the 580 cycle run. The results for both etched wafers resemble each other. Optical profilometry confirmed that 300 micron depth was achieved after 550 cycles with the initial deposition of 10 microns of SPR-2207. We were unable to determine if a thin layer of photoresist still existed on the surface because accurate surface measurements could not be taken with the available equipment. These etching experiments are used to understand the physical profile of the etched wafers and to characterize the NPS

equipment. The data suggests that 550 cycles is sufficient to etch a depth of 300 microns with 10 microns of photoresist.

THIS PAGE INTENTIONALLY LEFT BLANK

CHAPTER 4:

Results and Analysis

4.1 Experiment 2: Carbonization

In order to verify whether the carbon soot coated THz sensor produces sufficient spectral emissivity for IR-based readout, dummy test samples were used to proxy the working detectors. These test samples were carbonized in order to increase the emissivity of the readout side of the detectors. The intention is to investigate the process of carbon deposition and the impact of this film on emissivity.

4.1.1 Carbonized Sample 1

This section will address the deposition of a carbon thin film layer on test samples via chemical vapor deposition. Before the growth of the carbon layer, it is important to note that the top (patterned) and bottom (ground plane) layer of the THz structures are composed of aluminum. Aluminum has a melting point of 660°C . Finding the “right” temperature in which to fabricate the carbon thin film while maintaining the integrity of the sensor is essential. It needs to be done under conditions that will not melt or oxidize or otherwise destroy the aluminum layers of the detector’s structure.

The calorimeter was used to find the melting point of a sacrificial proxy test sample. The melting point will determine the furnace temperature for carbonization. Preparation of a test sample included the deposition and patterning of a 10 nm thin film of aluminum on a wafer initially composed of Si/SiO_2 . Aluminum was deposited with the Angstrom COVAP II, a deposition system for metals. The sample was placed on a crucible in the calorimeter for thermogravimetric analysis. The results can be seen in Figure 4.1

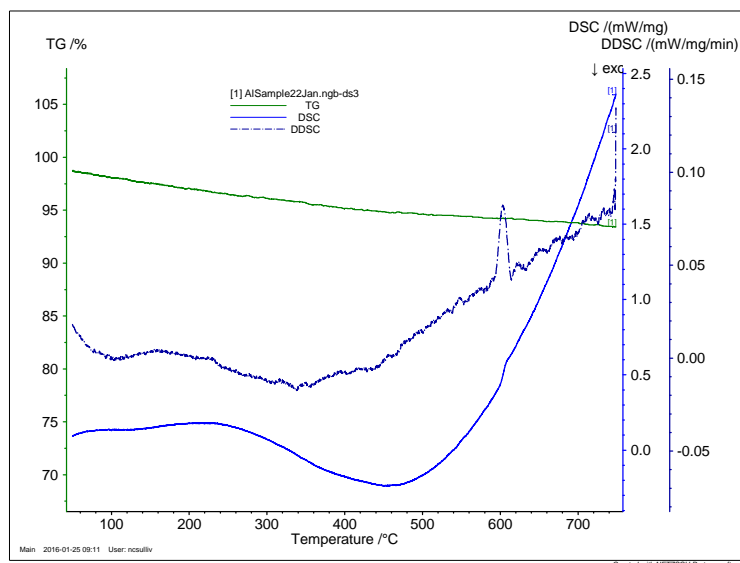


Figure 4.1: Thermogravimetric Analysis data obtained from the calorimeter. The green line is the thermogravimetry line, the dark blue line is the differential scanning calorimeter line, and the lighter blue line is the derivative differential scanning calorimeter line. The peak in the blue line shows the phase change (i.e., melting point).

Thermogravimetry (TG) line in Figure 4.1 shows no significant mass loss. For example, mass loss would be depicted on the graph as a large spike and would occur if there was oxidation, not applicable in this case. The differential scanning calorimeter (DSC) line shows a dip, probably due to residual SPR as dips are usually caused by polymers. There is a small protrusion on the DSC. This protrusion is more pronounced in the derivative differential scanning calorimeter (DDSC) line which equates to the point in which the sample has changed phase. This point was evaluated using Proteus software which showed that the start of the peak was at approximately 580°C and the top of the peak was at 603°C . The way in which the calorimeter was calibrated for aluminum could be the reason why the peak occurred before the well established melting point of aluminum, 660.3°C . The calorimeter was calibrated for aluminum by placing a bulk piece of aluminum in the crucible. This calibration measurement was compared to a nano-scale film of aluminum. The different scales might

have resulted in the shift of the peak to the left. Since the peak which determines melting point was at around 600°C , the furnace temperature for carbonization should be below this value to maintain the integrity of the THz device. We will use a value of 550°C .

Subsequently, another proxy sample is fabricated with the same raw materials, Si/ SiO_2 /Al. A catalyst for carbon, iron, is deposited on top of the aluminum layer. The catalyst facilitates carbon adhesion to the surface of the sample. We took an SEM image prior to carbonization Figure 4.2.

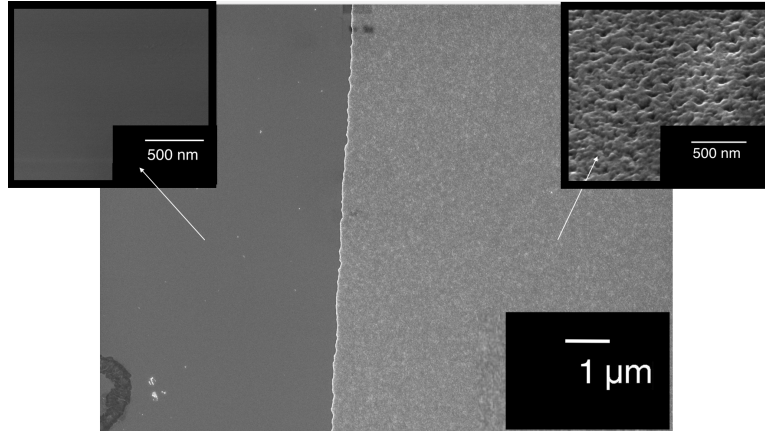


Figure 4.2: A SEM image at 5kV of a sample structure to be carbonized. The left hand side is smooth (shown in the inset) and composed of Si/ SiO_2 /Fe. The right hand side's surface is rough (shown in the inset) and is composed of Si/ SiO_2 /Al/Fe. Source: [30]

Since the aluminum was patterned, which mimics the aluminum pattern on the actual THz device, there are sections of the wafer that do not have aluminum. Figure 4.2 shows two sections of the sample. The left side of the sample is composed of Si/ SiO_2 /Fe and exhibits a smooth surface. The right side of the sample is composed of Si/ SiO_2 /Al/Fe and depicts a rough surface. Although there is a uniform layer of Fe, carbon deposit can be preferential to either side. The initial topology of the sample could also affect the way in which carbon is deposited. Therefore, it is important to image both areas of the proxy sample. All consecutive Figures are split into two sides, and for clarification the side with and without aluminum is identified.

Results and Analysis

The sample was carbonized at 550°C . See Appendix B for the carbonization steps. Three gases are used for carbonization: ethylene, oxygen, and nitrogen. The ethylene and oxygen react driving the system to make water and leaving behind carbon. This process exploits the “Le Chatelier’s Principle” where we increased the amount of hydrocarbon fuel relative to the amount of oxygen. This process creates more carbon because the reactive hydrogen more readily combines with the deprived oxygen, leaving the carbon behind. The carbon reacts with the catalyst and is then deposited on the device. The resulting sample was imaged with the SEM given in Figure 4.3.

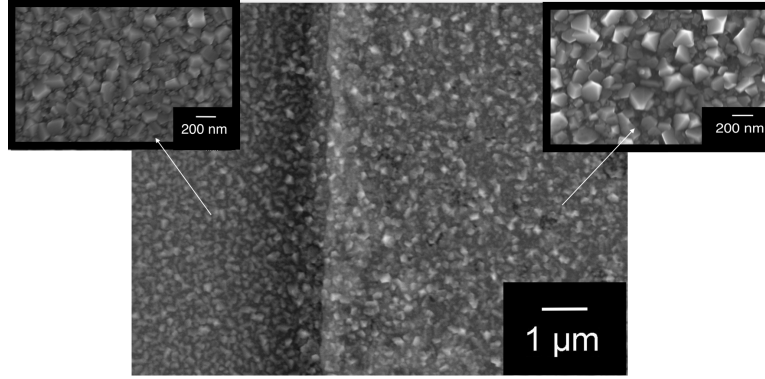


Figure 4.3: A SEM image at 5kV of a sample structure that has been carbonized. The left hand side is composed of $\text{Si}/\text{SiO}_2/\text{Fe}/\text{C}$. The right hand side is composed of $\text{Si}/\text{SiO}_2/\text{Al}/\text{Fe}/\text{C}$. The enlarged subsection of the image are there to show the carbon nanostructures that are present on each side. Source: [30].

Figure 4.3 shows that there are nano-crystalline structures on both sides of the sample. These carbon nanostructures (CNS) could not have originated from a pre-existing rough surface because the original sample imaged in Figure 4.2 shows that one side began as a smooth surface. These nano-crystalline structures resemble soot with a predominately graphitic structure. Carbon nanoparticles from soot are made up of lots of different sizes and exhibit a rough surface. The average size of a single crystal from this experiment is 87 nm.

Although, visually it looks as though carbon has been deposited, further analysis

is necessary to verify the presence of carbon vice some other trace element or the presence of a phase change. Therefore, we conducted an elemental analysis of the sample, namely energy dispersive X-ray microanalysis (EDX or equivalently EDS). Figure 4.4 portrays the results of the elemental analysis.

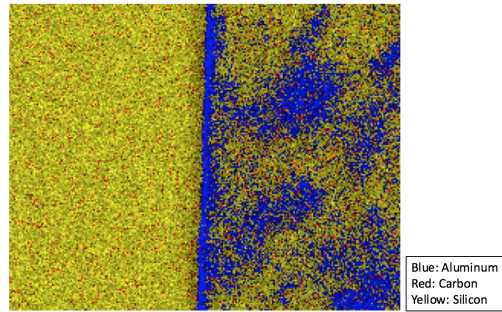


Figure 4.4: EDS (1500x) image of the elemental breakdown of the carbonized thin film. The legend to the right depicts the elements present. The Figure gives an overall picture of the quantities of each element within the sample. Source: [30].

Figure 4.4 shows overlays of three different elements: carbon, silicon, and aluminum. The figure gives an overall picture of the relative quantities of each element within the sample.

Table 4.1: EDS Data from the Right Hand Side of Figure 4.3.

Element	Weight % by Element	Atomic % by Element
C(K)	01.97	03.95
O(K)	19.02	28.72
Al(K)	00.60	00.54
Si(K)	76.88	66.13
Fe(K)	01.53	00.66

EDS data from the right hand side of sample Si/ SiO_2 /Fe/C. The element has an associated number, K, which indicates the series frequencies described in the EDS section. Source: [30]. S. Menon, private communication, 2016.

Table 4.2: EDS Data from the Left Hand Side of Figure 4.3.

Element	Weight % by Element	Atomic % by Element
C(K)	02.04	04.10
O(K)	18.66	28.20
Al(K)	05.11	04.58
Si(K)	72.48	62.38
Fe(K)	01.71	00.74

EDS data from the left hand side of sample $\text{Si}/\text{SiO}_2/\text{Al}/\text{Fe}/\text{C}$. The element has an associated number, K, which indicates the series frequencies described in the EDS section. Source: [30]. S. Menon, private communication, 2016.

Along with Figure 4.4, EDS provides tabulated results on each elemental composition and corresponding weight percentages and atomic percentages. The atomic weight shows the proportion of decomposition of each element in the sample. In Table 4.1 and Table 4.2, the main elements are silicon and oxygen and each element are associated with the first shell (K). K lines come from the first shell, L lines come from the second shell, and M lines come from the third shell. Section 2.2.1, which precedes this section, elaborated on the series frequencies for each X-ray transition.

Another important capability of EDS is the software's ability to give a graphical depiction of the composition of the surface of the sample. Figure 4.5 displays the resulting spectrum with peaks at characteristic energies that correspond to the element present. EDS X-ray line data (peaks) provide semi-quantitative elemental composition information because the accuracy of the numbers gives us a good sense of the proportions of each element, but cannot be taken to be exact. Moreover, the identification of the peaks can sometimes be quite challenging. For a peak to be statically valid, it must exceed the noise in the corresponding background by a large factor.

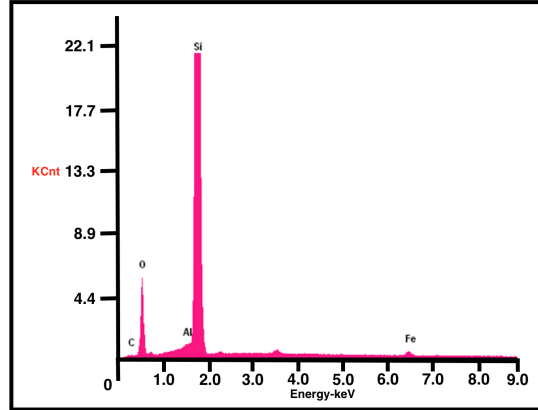


Figure 4.5: X-ray mapping of elements obtained of the carbon thin film from the left hand side of the sample composed of Si/ SiO_2 /Al/Fe/C. 22.1k counts were taken. 5 elements were identified, C, O, Si, Fe. Weak peaks coincide to Al and C. Source: [30].

Accelerating voltages of 20 keV are used in Figure 4.5 which increases the size of the interaction volume because X-rays are generated from very deep in the interactive region [21]. With this said, even by increasing the accelerating voltages, EDS only gives a surface analysis and does not represent the total composition of the target. Thus, using EDS to verify the deposition of carbon on the surface is valid. A constraint to elemental analysis is that EDS typically cannot detect elements that have an atomic number below Na, i.e., carbon [31]. The limit of detection for EDS in bulk material is about 0.1 weight %, and generally can achieve limits of detection of 100 ppm [32]. This threshold determines the lowest concentration of an element that might be detectable. According to EDS data, the carbon *weight%* is at $\sim 2\%$ which is 20,000 ppm ($0.001\% = 1$ ppm), well above 0.1 weight %. The ppm levels of carbon may not exclusively yield a conclusive quantitative analysis.

4.1.2 Carbonized Sample 3

The exact same procedure for carbonization (Appendix A) was used on two more proxy samples. One sample was a duplicate of the carbonized sample 2 in order to verify the former results. The results from the carbonized sample are shown in Figure 4.6

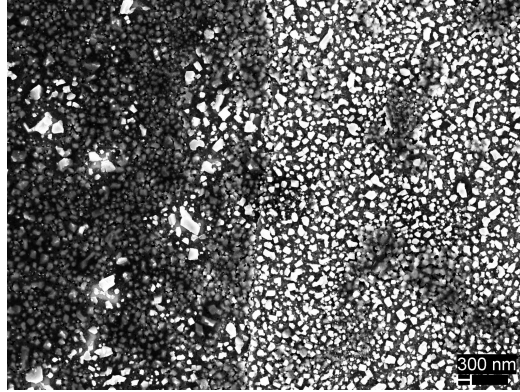


Figure 4.6: Third Carbonized Sample with Fe. SEM image is at 10K magnification. Carbon crystalline structures are depicted. Right side of the sample has aluminum. Source: [30].

Visually, the results from sample 2 and 3 (Figure 4.6 vs Figure 4.3) are similar. The left side of the sample is composed of $\text{Si}/\text{SiO}_2/\text{Fe}$. The right side of the sample is composed of $\text{Si}/\text{SiO}_2/\text{Al}/\text{Fe}$. There are nano-crystalline structures on both sides of the sample. To verify whether these nano-crystalline structures are composed of carbon, EDS was conducted and the results are depicted in Figure 4.7 and corresponding Table 4.3 and Table 4.4.

Table 4.4: EDS Data from Left Hand Side of Figure 4.6.

Element	Weight % by Element	Atomic % by Element
C(K)	06.92	13.28
O(K)	17.46	25.17
Al(K)	00.62	00.53
Si(K)	73.58	60.43
Fe(K)	01.42	00.59

EDS data from left hand side of second sample $\text{Si}/\text{SiO}_2/\text{C}$. The element has an associated number, K, which indicates the series frequencies described in the EDX section. Source: [30]. S. Menon, private communication, 2016.

Table 4.3: EDS Data from Right Hand Side of Figure 4.6.

Element	Weight % by Element	Atomic % by Element
C(K)	05.81	11.29
O(K)	17.46	25.46
Al(K)	04.58	03.96
Si(K)	70.53	58.61
Fe(K)	01.63	00.68

EDS data from right hand side of the second sample, $\text{Si}/\text{SiO}_2/\text{Al}/\text{C}$. The element has an associated number, K, which indicates the series frequencies described in the EDX section. Source: [30]. S. Menon, private communication, 2016.

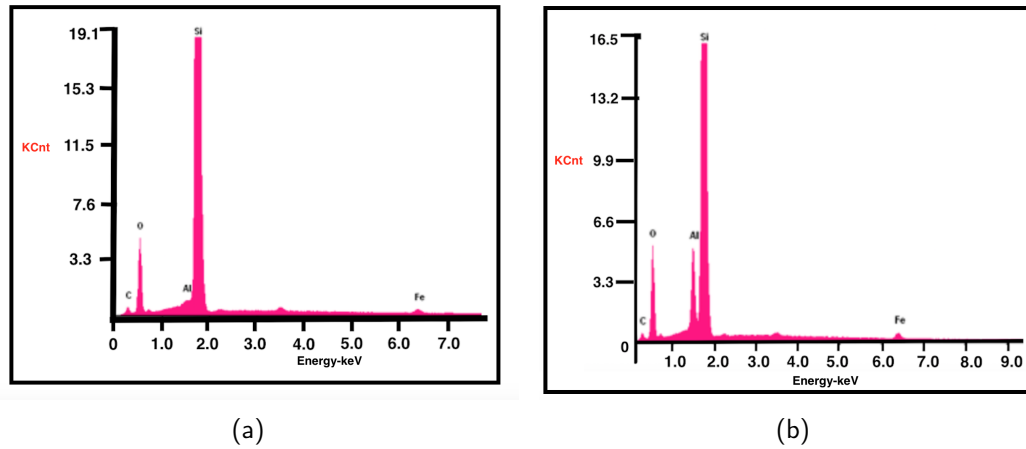


Figure 4.7: (a) Graphical illustration of EDS data obtained of carbon thin film elemental breakdown from Figure 4.6.(b) The left hand side of the sample contains trace amount of Al. Carbon is also shown as a weak peak and does not exceed the noise corresponding to the background. Source: [30].

Figure 4.7 gives a graphical illustration of the elements in Figure 4.6. Table 4.3 and Table 4.4 are tables of weight percentage by element that are gathered from Figure 4.7. Weight percentage determines the ppm value of the element. Carbon has a ppm value of $\sim 64,000$ ppm. This data leads to the conclusion that carbon has been deposited on the sample.

4.1.3 Carbonized Sample 4

The last sample that was carbonized had no iron in order to verify whether Fe was a necessary component for carbon deposition. This approach also allowed us to examine whether the exposed Al plays a role (i.e, serves as a catalyst) in carbon deposition. The second sample placed in the furnace to be carbonized was composed of Si/ SiO_2 /C on the right hand side and Si/ SiO_2 /Al/C on the left hand side. No Fe was deposited on this proxy sample. The results are shown in Figure 4.8

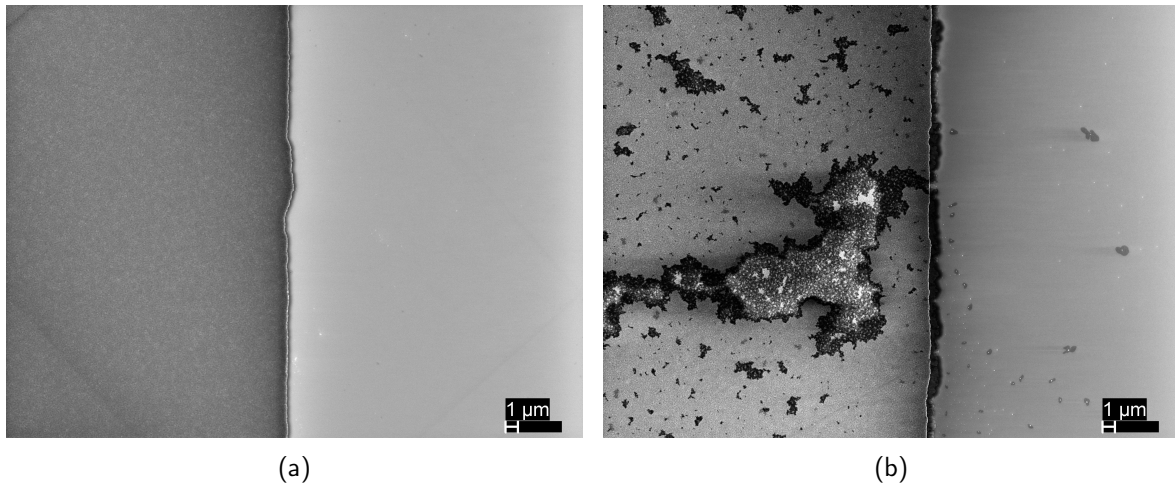


Figure 4.8: (a) SEM image (10k magnification at 5kV) of a sample without carbon and without Fe. (b) SEM image (10kX at 5kV) of a sample with carbon and without Fe. Source: [30].

Table 4.5: EDS Data from Right Hand Side of Figure 4.8.

Element	Weight % by Element	Atomic % by Element
C(K)	0.58	1.18
O(K)	17.62	26.82
Al(K)	0.31	0.28
Si(K)	80.15	69.62

EDS data from right hand side of the second sample, Si/ SiO_2 /C. The element has an associated number, K, which indicates the series frequencies described in the EDX section. Source: [30]. S. Menon, private communication, 2016.

Table 4.6: EDS Data from Left Hand Side of Figure 4.8.

Element	Weight % by Element	Atomic % by Element
C(K)	1.81	3.65
O(K)	17.72	26.82
Al(K)	3.95	3.5
Si(K)	76.52	66

EDS data from left hand side of second sample Si/*SiO*₂/Al/C. The element has an associated number, K, which indicates the series frequencies described in the EDX section. Source: [30]. S. Menon, private communication, 2016.

Figure 4.8 illustrates no deposition on the right hand side and an elongated black structure on the left side. Table 4.5 and Table 4.6 give weight percentages and atomic percentages illustrating the proportions of each element. Singular EDS analysis probing for carbon residue was conducted on the elongated black structure shown on the left hand side in Figure 4.8b. EDS reported no trace element of carbon was found. Therefore, the black structure must be from contamination because it has been out of the clean room for so long. It can also be concluded that without the addition of a catalyst, such as Fe, Ni, or Cr, carbon will not bind to the sample.

Results and Analysis

Although the exact amount of carbon cannot be determined using elemental analysis, a comparison can be made between carbonized sample 3 and 4's relative carbon content. Looking specifically at the proportion of decomposition of carbon from Table 4.3, Table 4.4, Table 4.5, and Table 4.6, a graph was generated representing the carbon weight percentages on the carbonized films (Figure 4.9).

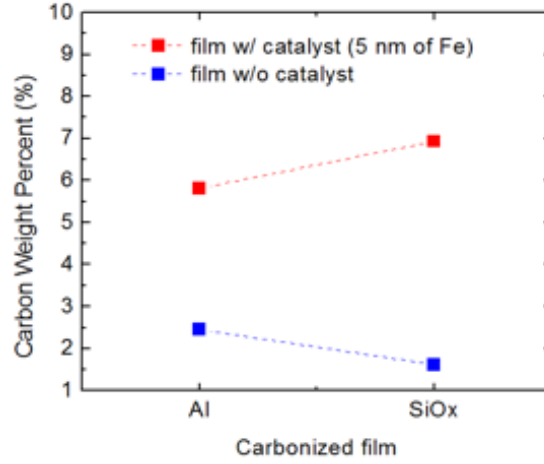


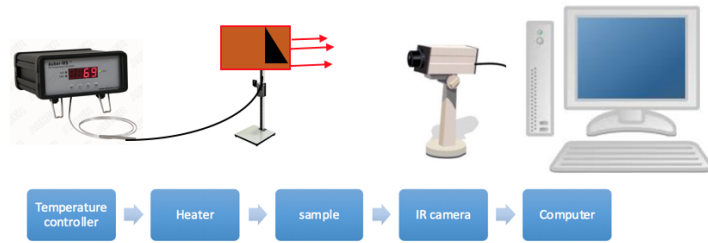
Figure 4.9: The red square represents the weight percent value of a carbonized sample that has catalyst. The blue square represents weight percent value of a carbonized sample without catalyst. The dotted lines are for visual aid only.

Figure 4.9 shows that the film with catalyst has a higher carbon weight percent than the one without catalyst. The graph also depicts carbon’s affinity for the SiO_2 side of the sample, if that side is carbonized.

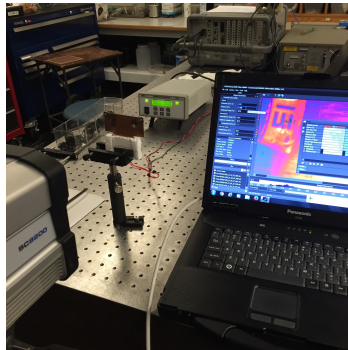
4.2 Experiment 3: Emissivity Test

Consider Kirchhoff’s law once again which states that for “an arbitrary body emitting and absorbing thermal radiation in thermodynamic equilibrium, the emissivity is equal to the absorptivity.” [16] Therefore, a good absorber is a good emitter. These qualities make a carbon thin film promising for applications such as heat radiation in materials for terahertz use. According to EDS, a carbon thin film was verified to have been deposited on samples with catalysts. The next step is to verify that the carbon film coating increases the emissivity of the samples. The optical scheme to produce emissivity results is described: first, samples are placed on the front side of a copper plate heater. The back side of the copper plate heater is connected by wires to a temperature controller which regulates the temperature on the copper frame. By increasing the temperature of the copper plate, less noise is collected in the IR

camera. The IR camera points to the sample and the sample is imaged using computer software, National Research IR. The software is able to record the temperature and respective emissivity values. The temperature is known, so by making adjustments to the emissivity parameter, the temperature is matched to the temperature on the temperature controller. In turn, this pin points the emissivity values. A picture of the setup is given in Figure 4.10.



(a)



(b)

Figure 4.10: (a) and (b) depict a scheme and picture of the setup of the optical scheme that was used to produce emissivity results. FLIR thermal infrared camera on the left records infrared radiation from the two samples placed on the stand. Wires are connected to the back plate of the copper stand which heat up the frame to which the samples are attached. The two samples are at the same temperature. The computer uses National Research IR software to determine emissivity values for each of the samples.

Figure 4.10 is a picture of the equipment used to produce emissivity results. At any one time, two samples can be placed on the copper frame. The copper frame is heated up to a desired temperature ($> 10^{\circ}\text{C}$ above room temperature). A FLIR

thermal infrared camera records the intensity of radiation from the samples in the infrared part of the electromagnetic spectrum ($3\mu m < \lambda < 5\mu m$) and sends that information to the electronics to convert it to a visible image. “The [camera] features an advanced, uncooled microbolometer FPA detector technology that delivers crisp, longwave images in a multitude of palettes that allow you to see temperature variations as small as $0.12^{\circ}C$.” [33] The FLIR thermal imaging software (Research IR) provides temperature readings for a given emissivity.

Fundamentally, the two samples on the copper frame are at the same temperature, but one has higher emissivity than the other. The one with lower emissivity will radiate less energy and the temperature reading on the IR camera will appear lower than the sample with higher emissivity. Therefore, by adjusting emissivity settings on the IR camera to match the actual temperature of the copper frame; we used temperatures of $35^{\circ}C$, $40^{\circ}C$, and $45^{\circ}C$, emissivity values were determined for each sample. In total, three samples were used, sample 3 and 4 from experiment 2 and a third sample was used as a control (or reference) emitter. The control is the emissivity sample that has no carbon and was used to normalize the changes in emissivity of the carbonized samples. The second sample was composed of $Si/SiO_2/Al/C$ and $Si/SiO_2/C$ and the third sample was composed of $Si/SiO_2/Al/Fe/C$ and $Si/SiO_2/Fe/C$. Table 4.7 show the values of emissivity for the 3 measured samples.

Table 4.7: Emissivity Values at 35°C, 40°C, and 45°C.

Temperature	35°C
Without Carbon	Emissivity
SiO_2	0.215
Al	0.13
With Carbon and Fe	Emissivity
SiO_2	0.24
Al	0.52
With Carbon without Fe	Emissivity
SiO_2	0.2
Al	0.245
Temperature	40°C
Without Carbon	Emissivity
SiO_2	0.215
Al	0.12
With Carbon and Fe	Emissivity
SiO_2	0.215
Al	0.55
With Carbon without Fe	Emissivity
SiO_2	0.205
Al	0.255
Temperature	45°C
Without Carbon	Emissivity
SiO_2	0.205
Al	0.009
With Carbon and Fe	Emissivity
SiO_2	0.21
Al	0.525
With Carbon without Fe	Emissivity
SiO_2	0.175
Al	0.205

Figure 4.11 is a graph representing the values for samples 3 and 4 separated by regions, Al and SiO_2 , obtained for 3 different temperatures.

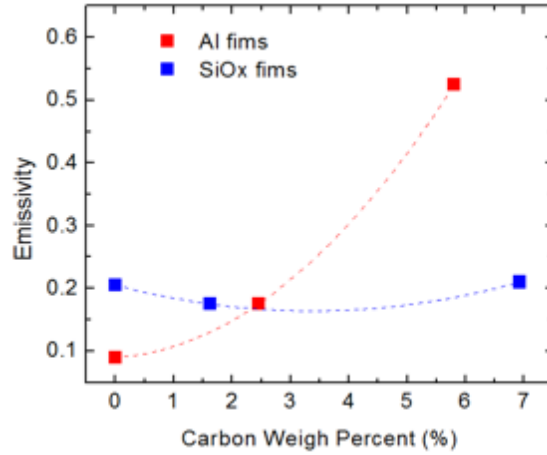


Figure 4.11: Graph of Emissivity Results. The control is used as a reference emitter. The carbonized samples were obtained from experiment 2. The tests were conducted at three different temperatures, 35°C, 40°C, and 45°C and at two different areas of the proxy sample. Each point is an average. One area of the sample contains Al (dotted line), and the other contains SiO_2 in their base layers (solid line).

In order to read the temperatures of small samples, a macro lens was used with the IR camera, which was not calibrated for that lens. Nonetheless, the main interest is not to obtain the absolute values, but the changes. In Figure 4.11, the aluminum film indicates that the emissivity values trend upward with larger weight percent. The highest value of emissivity is attributed to the side with catalyst and aluminum which emphasizes the role the catalyst plays in carbon adhesion. Although, the carbon weight percent increased on the SiO_2 side of the sample, the values of emissivity stayed relatively constant. Future work will have to be dedicated to understanding this phenomenon. Nonetheless, the results of this research demonstrate that carbon on the aluminum iron side of samples increases the emissivity of the sample. In addition, carbon can be a promising choice for improving IR emissivity.

CHAPTER 5:

Conclusions and Future Research

5.1 Conclusion

Throughout this study, we used different micromachining techniques, such as deposition of carbon and etching of silicon wafers. These techniques led to a new design for the THz sensor which promises improved performance. The etching experiment of the silicon wafers was used to understand the physical profile of the etched wafers and to characterize the NPS equipment. This characterization is helpful for those who will perform fabrication experiments in the NPS clean room. Furthermore, we have developed a simplified technique to perform THz imaging. Using this technique, we show that carbon thin films produce sufficient spectral emissivity for IR-based readout. We also determined that pure aluminum could not be used as catalyst for CVD of carbon. An iron catalyst is presently required. Similarly, a study used a mixture of Ni/Al because the researchers found pure Ni (without the Al catalyst) produced no carbon nanotube growth [34]. The additional layers of carbon and catalyst increase steps in the fabrication process and increase the thermal time constant ($\tau = C/G$). Further research will have to be done to determine the effects the additional layers will have on responsivity and detectivity. However, the advancement in the spectral emissivity for IR-based readout due to the carbon film is appropriate for the optical application we seek, lens production that can be screwed onto a regular IR camera as an attachment. In conclusion, this study provides a viable method to fabricate thin carbon films at low temperatures for IR-based readout.

5.2 Future Research

One way to proceed with future research would be to carbonize similar proxy samples at different temperatures. Although this experiment used a temperature of 550°C , other research has developed low-temperature growth of aligned carbon nanotubes by chemical vapor deposition [35]. The researchers used a silicon substrate coated with a metal catalyst, which is similar to our setup, to probe for carbon nanotube growth.

These researchers found that at 400°C the nanotubes were not made up of perfect graphite, but mixed with soot [35]. This mixed soot would be fitting for the THz sensors. Therefore, CVD could potentially be done at temperatures as low as 400°C . Therefore, future research would look at carbon content as a function of temperature.

The next step would be to investigate the dependence of carbon on the catalyst thickness. Once the ideal amount of catalyst is deposited, the sample would be carbonized and the amount of carbon measured. Afterwards, dependence of emissivity on the carbon content could be determined.

In conclusion, actual devices would need to be carbonized in order to discern whether the modifications listed above would be suitable. If the THz detectors could be successfully carbonized, the next step would be to place the device in the optical scheme previously laid out to determine their performance. Properties such as responsivity and detectivity would need to be calculated to quantify the performance of the terahertz sensors. Each of these future research avenues would refine the findings presented here and help to provide a better understanding of terahertz imaging in the IR spectrum.

APPENDIX A:

Bosch Etch

This appendix shows the Bosch etching process.

A.1 Bosch Etching

This section explains each stage in the process of Bosch etching at the Navy Post-graduate School. The following is procedure to prepare the sample prior to Bosch etching

A.1.1 Preparing the Wafer

The following procedure was followed

1. Deposit SPR-2207 at 2000 rpm with 200 ramp time.
2. Bake for 120 seconds.
3. Place in mask aligner for photolithography.
4. Wait 35 min, post-exposure bake ($115^{\circ}\text{C}/90\text{sec}$), develop in CD-26 as needed, rinse in water, and dry.
5. Remove the edge bead.
6. Measure the thickness using contact profilometer and filimetrics.

At this point the wafer is ready to be Bosch etched.

A.1.2 Bosch Procedure

The following procedure was followed

1. Set chiller temperature to 15°C .
2. Press STOP on the main screen under cycling loadlock pumping.
3. Vent the chamber.
4. Load the wafer. Push wafer to guide screws and check that the edge bead has been removed.
5. Press stop and evacuate.

6. Load the recipe. Configure the Oxford etcher to Bosch etch for a 9 sec etch rate and a 3 sec deposition rate. Set the number of cycles.
7. Press Run.

A.1.3 Follow on Procedure

1. Press ok on the process status when prompted.
2. Press stop on cycling loadlock pumping.
3. Vent the chamber.
4. Remove the wafer.
5. Press stop, evacuate, and cancel to end the process.

APPENDIX B:

Carbonization

This appendix shows the carbonization process.

B.1 Carbonization

This section explains each stage in the process of carbonization in the furnace at the Navy Postgraduate School. Figure B.1 displays the preparation of the sample prior to placing it in the furnace

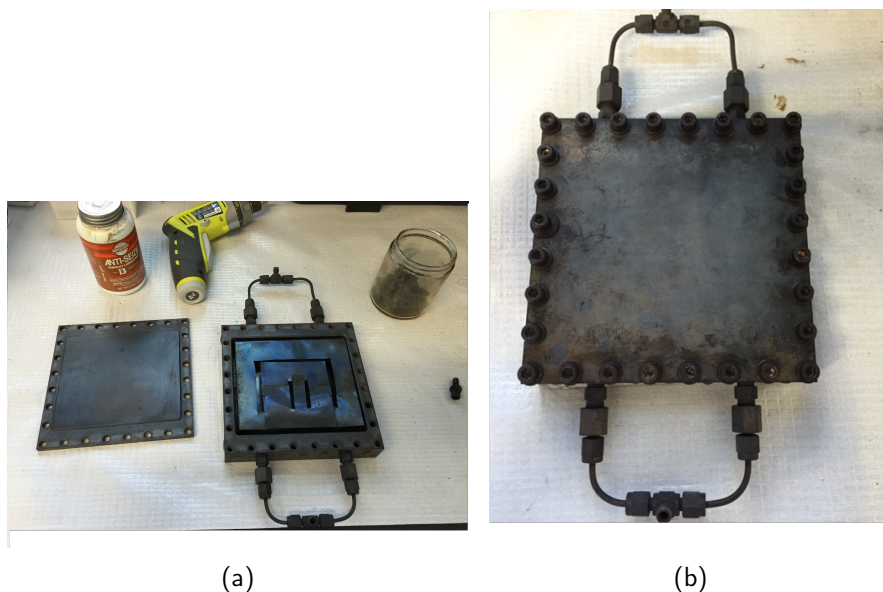
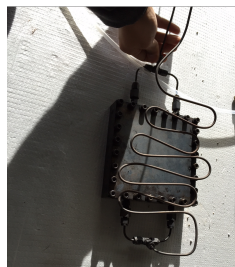


Figure B.1: (a) The mold used for carbonization. The component on the right is the mold itself. The two inlets and two outlets on the mold are for gas flow. The sample is placed at the bottom of the mold. A thin metal layer is placed on top which is used to create a more homogenous flow of the gasses around the sample. The component on the left will go on top of the mold. The enclosure is placed on and screwed down. (b) shows the prepared mold with sample.



(a)



(b)

Figure B.2: (a) Wires are placed on the inlet and outlet of the mold. (b) The furnace used for carbonization. The power button is located on the left bottom portion of the furnace. The temperature set point and indicator is located on the right adjacent to the power button. The volumetric flask that measures flow is to the right of the furnace.



(a)



(b)

Figure B.3: (a) The hole in the front of the furnace is the location gas flows in and out. The inlet is connected to the gas flow meter used for carbonization. (b) The gas flow meter. The flow meter is located to the left. The tank on the closest to the left is nitrogen, the tank in the middle is ethylene, and the tank to the right is oxygen.

Figure B.1a delineates the mold in which the sample is placed. Then, the mold is arranged in the furnace (Figure B.2). Two gas lines are connected to either end of the mold and run out through the center hole in the furnace to the gas flow meter (Figure B.3) and to the exhaust. The furnace is turned on and set to a specific temperature. In our case, we used 500° C.

B.1.1 Procedure

The following procedure was then followed

1. Press option 2 extended display to access the control of flow of gases.
2. Flush the system with nitrogen at 300 sscm for 30 min. On the monitor, press the on button and then the all button to get the flow going. Status should read on. Check the flow meter next to the tank. Normally, the flow meter is at 60ml.
3. Increase nitrogen to 330 sscm.
4. Open the ethylene tank and set flow to 50 sscm.
5. Open the oxygen tank and set flow to 5 sscm.
6. Every 5 minutes increase the flow of oxygen by increments of 5 sscm until flow has reached 50 sscm.
7. Once 50 sscm of oxygen is flowing in the system, mark time for one hour.
8. After one hour, turn furnace off (flip power button to down position).
9. Stop the flow of oxygen first on the flow controller and then close the oxygen tank.
To stop the flow of oxygen set the set point to 000 sscm and turn status off.
10. Stop the flow of ethylene. To stop the flow of ethylene set the set point to 000 sscm and turn status off.
11. For nitrogen, decrease the flow to 10 sscm and leave running over night to cool off. The flow controller panel should read at the bottom “flow on” with 10 sscm N_2 actually flow.
12. Place block in furnace to allow for quicker cooling.

B.1.2 Follow on Procedure

The next day the following procedure was performed

1. Turn nitrogen flow off. To stop the flow of nitrogen set the flow to 000 sscm and turn status off.
2. Verify that all flow meters have been turned off.
3. Press exit on the monitor.
4. Turn off button in the back of monitor.
5. Disassemble the mold to obtain sample.

THIS PAGE INTENTIONALLY LEFT BLANK

List of References

- [1] A. Morris. (2014). Team demonstrates continuous terahertz source at room temperature. [Online]. Available: <http://www.mccormick.northwestern.edu/news/articles/2014/06/team-demonstrates-continuous-terahertz-sources-at-room-temperature.html>. Unpublished.
- [2] U. of Fukui Research center for development for Far-Infrared Region. (n.d.). Thz frequency region. [Online]. Available: http://fir.u-fukui.ac.jp/thzlab/index_files/Eng_THz_TDS.htm. Accessed May 05, 2016.
- [3] J. Lucas. (Mar. 26, 2015). What is infrared. [Online]. Available: <http://www.livescience.com/50260-infrared-radiation.html>. Accessed May 05, 2016.
- [4] “Photonics,” class notes for PH4272, Dept. of Phys. Naval Postgraduate School, fall 2015.
- [5] B. T. Kearney, “Enhancing microbolometer performance at terahertz frequencies with metamaterial absorbers,” Ph.D. dissertation, Dept. Physics, Naval Postgraduate School, Monterey, CA, 2013.
- [6] D. Grbovic, A. Fabio, G. Karunsiri, and J. Newman, “Metal-organic hybrid metamaterial thz imaging band translators,” *SPIE*, vol. 9476, pp. 1–8, 2015.
- [7] “Microelectromechanicalsystems,” class notes for PH3280, Dept. of Phys. Naval Postgraduate School, summer 2015.
- [8] W. Wolfe and P. Kruse. (n.d.). Thermal detectors. [Online]. Available: http://photonics.intec.ugent.be/education/IVPV/res_handbook/v1ch19.pdf. Accessed February 24, 2016.
- [9] B. K. F. Alves, D. Grbovic, and G. Kuranasiri, “Al/sio/a; single and multiband metamaterial absorbers for terahertz sensor applications,” *Optical Engineering*, vol. 52 no.1, pp. 0 138 011–0 138 018, Jan. 2013.
- [10] F. Alves, D. Grbovic, and G. Kuranasiri, “Investigation of microelectromechanical systems bimaterial sensors with metamaterial absorbers for terahertz imaging,” *Optical Engineering*, vol. 53 no. 9, pp. 0 971 031–0 971 039, Sep. 2014.
- [11] J. Carnes and P. Levine. (Oct. 7, 1975). Interlaced readout of charge stored in charge-coupled image sensing array. [Online]. Available: http://www.engineeringtoolbox.com/emissivity-coefficients-d_447.html. Accessed May 05, 2016.

- [12] “Intro to Space Environment,” class notes for PH2514, Dept. of Phys. Naval Postgraduate School, winter 2016.
- [13] Elsevier. (n.d.). New research shows candle soot can power the lithium batteries in electric cars. [Online]. Available: <http://phys.org/news/2015-10-candle-soot-power-lithium-batteries.html>. Accessed Mar. 31, 2016.
- [14] M. Bottini and T. Mustelin, “Nanosynthesis by candlelight,” *Nature*, vol. 2, pp. 599–600, Oct. 2007.
- [15] U. of Cambridge. (n.d.). Silver from soot. [Online]. Available: <http://www.thenakedscientists.com/HTML/experiments/exp/silver-from-soot/>. Accessed Apr. 08, 2016.
- [16] M. Clavey. (n.d.). Kirchhoff’s law of thermal radiation. [Online]. Available: <http://thermalvisionresearch.co.uk/kirchhoffs-law-of-thermal-radiation/>. Accessed Mar. 21, 2016.
- [17] FLIR. (2015 Oct.). Use low-cost materials to increase target emissivity. [Online]. Available: <http://www.flir.com/science/blog/details/?ID=71556>. Accessed Apr. 07, 2016.
- [18] T. E. ToolBox. (n.d.). Emissivity coefficients of some common materials. [Online]. Available: http://www.engineeringtoolbox.com/emissivity-coefficients-d_447.html. Accessed May 05, 2016.
- [19] T. Giebultowicz. (Spring 2009). X-ray scattering and moseley’s lab. [Online]. Available: physics.oregonstate.edu/~tgiebult/COURSES/ph314Moseleylab. Accessed Feb. 24, 2016.
- [20] “Lab 2 - moseley’s law,” class notes for Physics 42, Dept. of Phys. Dartmouth, fall 1996, accessed Feb. 24, 2016. [Online]. Available: <http://www.dartmouth.edu/~physics/labs/writeups/moseleys.law.pdf>
- [21] B. Hafner. (n.d.). Energy dispersive spectroscopy on the sem: A primer. University of Minnesota - Twin Cities. [Online]. Available: http://www.charfac.umn.edu/instruments/eds_on_sem_primer.pdf. Accessed Feb. 24, 2016.
- [22] D. Grbovic, A. Fabio, G. Karunsiri, and N.Lavrik, “Cnms-011 2015-r55 project,” 2015, unpublished.
- [23] D. Grbovic *et al.*, “Metal-organic hybrid metamaterial thz imaging band translators,” *SPIE*, vol. 9476, May 2015.

- [24] MEMS and N. Exchange. (n.d.). Etching process. [Online]. Available: <https://www.memsnet.org/mems/processes/etch.html>. Accessed Feb. 24, 2016.
- [25] “A deep silicon rie primer bosch etching of deep structures in silicon,” University of Alberta, 2009 Apr., accessed Feb. 24, 2016. [Online]. Available: http://www.nanofab.ualberta.ca/wp-content/uploads/2009/03/primer_deepsiliconrie.pdf
- [26] P. D. Rack. Plasma etching outline.
- [27] AZoNano. (n.d.). Dry etching of inp based materials using high density inductively coupled plasma (icp) by oxford instruments plasma technology. [Online]. Available: <http://www.azonano.com/article.aspx?ArticleID=2716>. Accessed Feb. 24, 2016.
- [28] D. Grbovic, private communication, 2015.
- [29] “PLA 501/600 data sheet,” Neutronix/Quintel, Morgan Hill, CA.
- [30] S. Menon, private communication, 2016.
- [31] J. Goodge. (n.d.). Energy-dispersive x-ray spectroscopy (eds). [Online]. Available: http://serc.carleton.edu/research_education/geochemsheets/eds.html. Accessed Feb. 25, 2016.
- [32] J. Goldstein *et al.*, *Scanning Electron Microscopy and X-Ray Microanalysis: A Text for Biologists, Material Scientists, and Geologists*, 2nd ed. Berlin, Germany: Springer, 1992.
- [33] U. of Capetown. (n.d.). Edx:precision and accuracy in edx analysis. [Online]. Available: <http://emu.uct.ac.za/training/sem-school/precision-and-accuracy-in-edx-analysis/>. Accessed Feb. 25, 2016.
- [34] C. He *et al.*, “Study of aluminum powder as transition metal catalyst carrier for cvd synthesis of carbon nanotubes,” *Elsevier*, vol. 441, pp. 266–270, Dec. 2006.
- [35] Y.-M. Shyu and F. C.-N. Hong, “Low-temperature growth and field emission of aligned carbon nanotubes by chemical vapor deposition,” *Elsevier*, vol. 72, pp. 223–227, 2001.

THIS PAGE INTENTIONALLY LEFT BLANK

Initial Distribution List

1. Defense Technical Information Center
Ft. Belvoir, Virginia
2. Dudley Knox Library
Naval Postgraduate School
Monterey, California